



Concentration-Gradient Prussian Blue Cathodes for Na-Ion Batteries

Pu Hu, Wenbo Peng, Bo Wang, Dongdong Xiao, Utkarsh Ahuja, Julien Réthoré, Katerina Aifantis

► To cite this version:

Pu Hu, Wenbo Peng, Bo Wang, Dongdong Xiao, Utkarsh Ahuja, et al.. Concentration-Gradient Prussian Blue Cathodes for Na-Ion Batteries. ACS Energy Letters, 2019, 5 (1), pp.100-108. 10.1021/ac-senergylett.9b02410 . hal-02436261

HAL Id: hal-02436261

<https://hal.science/hal-02436261v1>

Submitted on 18 Nov 2020

HAL is a multi-disciplinary open access archive for the deposit and dissemination of scientific research documents, whether they are published or not. The documents may come from teaching and research institutions in France or abroad, or from public or private research centers.

L'archive ouverte pluridisciplinaire **HAL**, est destinée au dépôt et à la diffusion de documents scientifiques de niveau recherche, publiés ou non, émanant des établissements d'enseignement et de recherche français ou étrangers, des laboratoires publics ou privés.



Distributed under a Creative Commons Attribution 4.0 International License

Concentration-gradient Prussian blue cathodes for Na-ion batteries

Pu Hu,[†] Wenbo Peng,[†] Bo Wang,[†] Dongdong Xiao,[‡] Utkarsh Ahuja,[†] Julien Réthoré,[§] and Katerina E. Aifantis,^{†}*

[†] Department of Mechanical and Aerospace Engineering, University of Florida, Gainesville, 32603, USA

[‡] Beijing National Laboratory for Condensed Matter Physics, Institute of Physics, Chinese Academy of Sciences, Beijing 100190, China

[§] Research Institute in Civil and Mechanical Engineering (Gem), CNRS UMR 6183 CNRS / Ecole Centrale de Nantes / Université de Nantes, F-44 321, Nantes, France.

AUTHOR INFORMATION

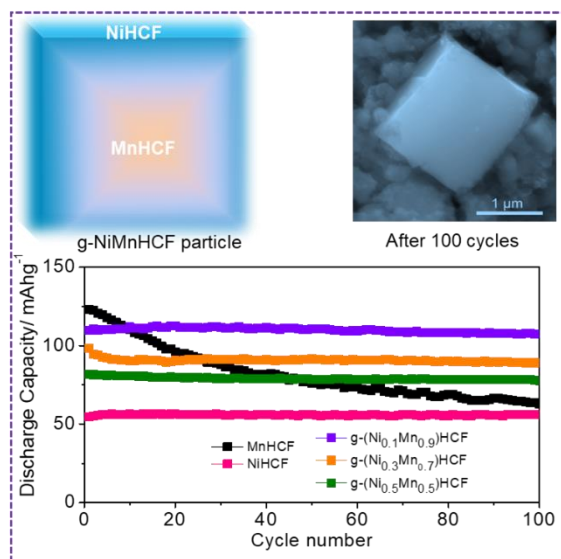
Corresponding Author

* Email: kaifantis@ufl.edu

ABSTRACT A concentration-gradient composition is proposed as an effective approach to solve the mechanical degradation and improve the electrochemical cyclability for cathodes of sodium-ion batteries. Concentration-gradient shell $\text{Na}_x\text{Ni}_y\text{Mn}_{1-y}\text{Fe}(\text{CN})_6 \cdot n\text{H}_2\text{O}$, in which the Ni content gradually increases from the interior to the particle surface, is synthesized by a facile co-

precipitation process. The as-obtained cathode exhibits an improved electrochemical performance compared to homogeneous $\text{Na}_x\text{MnFe}(\text{CN})_6 \cdot n\text{H}_2\text{O}$, delivering a high reversible specific capacity of 110 mA h g^{-1} at 0.2 C and outstanding cycling stability (93% retention after 1000 cycles at 5 C). The improvement of electrochemical performance can be attributed to its robust microstructure that effectively alleviates the electrochemically induced stresses and accumulated damage during sodiation/desodiation and thus prevents the initiation of fracture in the particles upon long term cycling. These findings render a prospective strategy to develop high-performance electrode materials for sodium-ion batteries.

TOC GRAPHICS



Sodium ion batteries (SIBs) have been gaining increased attention as a potential energy storage device.¹⁻⁴ Compared to lithium, sodium is available abundantly and relatively inexpensive, thereby reducing the cost of the electrode material. Moreover, sodium has similar electrochemical properties to lithium and maintains a good reversibility in a variety of host materials. Hence,

significant efforts are being undertaken to commercialize SIBs for large-scale energy storage (EES) systems. Recently, a SIBs system with a power rating of 30 kW/100 kWh was installed in China.⁵ Nevertheless, long-term cycling stability of SIBs still remains a challenge.

Mechanical degradation is commonly observed in both cathode and anode materials of Li-ion batteries, which is the leading contributor of capacity decay of batteries.⁶⁻¹⁰ Fracture of the electrodes is caused by volume expansions, phase transformations, formation of oxygen vacancies and surface corrosion of the active materials upon intercalation.¹¹⁻¹⁴ Such mechanisms have been experimentally observed in cathode materials ($\text{LiNi}_{1/3}\text{Mn}_{1/3}\text{Co}_{1/3}\text{O}_2$, LiMn_2O_4 , LiFePO_4) for LIBs,¹⁴⁻¹⁶ and although their volumetric expansions are less than 10% (2.0% expansion along c direction for $\text{LiNi}_{1/3}\text{Mn}_{1/3}\text{Co}_{1/3}\text{O}_2$ ¹⁷, 7% expansion for LiFePO_4 ¹⁸, and 6.77% expansion for LiFePO_4 ¹⁹), repeated lattice expansion and contraction during electrochemical cycling leads to accumulation of damage which subsequently leads to mechanical degradation of the electrode. Due to the larger ionic radius of Na^+ from Li^+ , the electrode during sodiation/desodiation is subjected to larger volumetric strains and more complicated multi-phase transformations than those during lithiation/delithiation.²⁰⁻²¹ This suggests that mechanical degradation may result in more severe damage in cathode materials during the charge/discharge process in SIBs. Our previous research revealed that the maximum effective von Mises stress in a layered-type TiS_2 cathode was four times higher during sodiation than lithiation and numerous cracks were observed with electron microscopy after continuous electrochemical cycling. Therefore, understanding the mechanical degradation as well as (de)sodiation-induced fracture of cathodes is essential in achieving long-term stability in SIBs. To date, a systematic investigation on the effect of the cathode mechanical properties to the electrochemical performance of SIBs is lacking.

Prussian blue and its analogues (PBAs) with a unique 3D open-framework are promising cathode materials for SIBs.²²⁻²⁴ These materials have a general formula of $A_xM_yFe(CN)_6 \cdot nH_2O$, abbreviated as MHCF, (A is the alkali cation and M is a divalent or trivalent transition metal), in which six-fold C-coordinated Fe and six-fold N-coordinated M are connected by CN ligands, forming Fe–C≡N–M linked open-frameworks and large interstitial sites. The wide channels and weak interaction between the Na^+ ion and the cyanide triple bonds in such a unique structure allows fast Na^+ diffusion. Among PBAs, $Na_xMnFe(CN)_6$ (MnHCF) exhibits a high redox potential and high theoretical capacity of 171 mAh/g, which is comparable to commercial $LiFePO_4$ cathodes in LIBs.²⁵⁻²⁸ However, a capacity decay is observed experimentally, as previous reports²⁹⁻³¹ show that only a 30% capacity retention is achieved after 200 cycles at 0.5 C in liquid electrolyte, which has been attributed to structural instabilities that take place during electrochemical cycling. Participation of both Fe and Mn sites in redox reactions results in lattice distortion and changes the C≡N bond length. Moreover, the structural instability of MnHCF is also caused by the crystal Jahn-Teller (J-T) distortion of $Mn^{3+} (t_{2g}^3e_g^1)$ ³² and volume changes ($\sim 8.5\%$)³¹ during cycling. In addition to structural changes, dissolution of Mn species in the organic electrolyte leads to surface corrosion of the electrode.²⁹ All these factors would be expected to contribute to local fracture and mechanical degradation of the PBA electrode, leading to capacity decay. It is known that Ni^{2+} is electrochemically inert in $Na_2NiFe(CN)_6$ (NiHCF) and Fe is the only redox active site, making the Fe–C≡N–Ni bond extremely stable. Earlier studies have shown that NiHCF undergoes zero lattice strain (volume change $\sim 0.29\%$) during sodiation/desodiation and displays excellent cycling stability (90% capacity retention over 1000 cycles).²⁷

In the present study a concentration-gradient composition is proposed as an effective approach to solve the mechanical degradation and improve the electrochemical cyclability for

cathodes of sodium-ion batteries. Concentration-gradient $\text{Na}_x\text{Ni}_y\text{Mn}_{1-y}\text{Fe}(\text{CN})_6 \cdot n\text{H}_2\text{O}$ (g- $\text{Na}_x\text{Ni}_y\text{Mn}_{1-y}\text{Fe}(\text{CN})_6 \cdot n\text{H}_2\text{O}$), in which Ni gradually increases while Mn decreases from the interior to the particle surface, is synthesized by a facile co-precipitation process. The NiHCF shell does not experience volume changes upon sodiation and was anticipated to increase the mechanical stability of the MnHCF rich core that undergoes volume changes upon cycling. Phase field modelling is employed to capture the internal stresses developed during cycling and correlate mechanical with electrochemical stability. In addition to testing the performance of these PBA materials in a half cell, a full cell was also fabricated and tested using either graphite or TiS_2 as the anode.

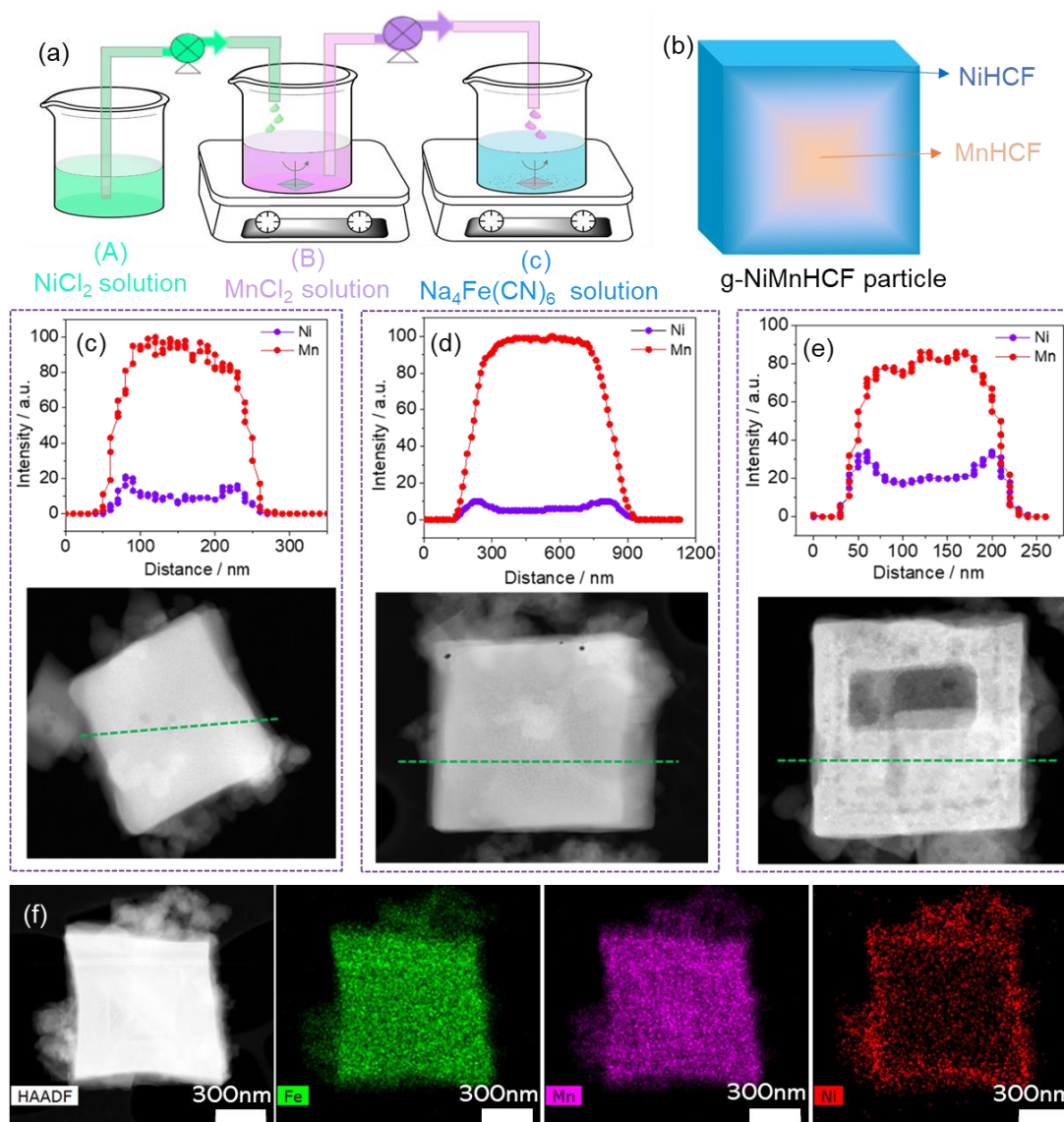


Figure 1 (a) Schematics illustrating the preparation of g-NiMnHCF. (b) Illustration of a gradient particle, where NiHCF gradually increases while MnHCF decreases from the interior to the particle surface, forming a core/shell structure. (c)-(e) STEM images and EDX linear scan for the typical gradient particles with different Ni/Mn ratios: (c) g-($\text{Ni}_{0.1}\text{Mn}_{0.9}$)HCF, (d) g-($\text{Ni}_{0.3}\text{Mn}_{0.7}$)HCF and (e) g-($\text{Ni}_{0.5}\text{Mn}_{0.5}$)HCF. (f) STEM images and element mapping for g-($\text{Ni}_{0.3}\text{Mn}_{0.7}$)HCF.

Concentration-gradient particles of g-(NiMn)HCF were prepared via a scalable co-precipitation process, as described in **Figure 1a**. Ni^{2+} solution was slowly pumped into the Mn^{2+} to obtain a mixture with increasing Ni^{2+} concentration. The resultant mixture of $\text{Ni}^{2+}/\text{Mn}^{2+}$ was precisely pumped into $\text{Na}_4\text{Fe}(\text{CN})_6$ solution to form a precipitate under constant magnetic stirring. As a result, concentration-gradient particles with a Ni-rich surface and Mn-rich core were obtained (Figure1b). By adjusting the molar ratio of Ni^{2+} and Mn^{2+} (1:9, 3:7, 1:1), a series of gradient $\text{Na}_x(\text{Ni}_y\text{Mn}_z)\text{HCF}$ with different stoichiometries were synthesized. Thermogravimetric analysis (TGA) (Figure S1) and ICP-OES (Table.S1) were carried out to determine the composition of the obtained materials, which were identified as $\text{Na}_{1.17}(\text{Ni}_{0.12}\text{Mn}_{0.88})[\text{Fe}(\text{CN})_6]_{0.79} \cdot 1.5\text{H}_2\text{O}$, $\text{Na}_{1.37}(\text{Ni}_{0.28}\text{Mn}_{0.72})[\text{Fe}(\text{CN})_6]_{0.84} \cdot 2.39\text{H}_2\text{O}$ and $\text{Na}_{1.81}(\text{Ni}_{0.59}\text{Mn}_{0.41})[\text{Fe}(\text{CN})_6]_{0.95} \cdot 3.3\text{H}_2\text{O}$. The molar ratio of Ni/Mn in these materials was found to be close to the molar ratio of $\text{Ni}^{2+}/\text{Mn}^{2+}$ mixture used in the synthesis. We denoted them as g-($\text{Ni}_{0.1}\text{Mn}_{0.9}$)HCF, g-($\text{Ni}_{0.3}\text{Mn}_{0.7}$)HCF and g-($\text{Ni}_{0.5}\text{Mn}_{0.5}$)HCF. Figure S2 shows the X-ray diffraction (XRD) patterns of the gradient materials as well as the homogeneous MnHCF and NiHCF. The splitting diffraction peaks for MnHCF at around 23.7° and 37.9° are a notable characteristic of monoclinic phases ($\text{P2}_1/\text{n}$ space group). From MnHCF to NiHCF, the diffraction peak shifted to a higher angle with increasing the Ni content in the materials. This is due to the radius of Ni^{2+} (0.69\AA) being smaller than that of Mn^{2+} (0.83\AA), leading to the shrinkage of the lattice for compounds with higher Ni contents. Fourier-transform infrared spectroscopy (FTIR) was performed to probe the chemical structure of the obtained materials. The absorption peak at 2085 cm^{-1} in FTIR (Figure S3) revealed the characteristic stretching vibration of the cyanide ($\text{Fe}-\text{C}\equiv\text{N}-\text{M}$, $\text{M}=\text{Mn, Ni}$) group. Since the electronegativity of Ni (1.91) is higher than Mn (1.55), the substitution of Ni with Mn could induce an inductive effect,

which lead to the blue shift of the peak. With increasing the Ni concentration, the absorption peak gradually shifted to a higher wavenumber.

Scanning transmission electron microscopy (STEM) was carried out to determine the local composition and distribution of transition metals within a single particle. All the particles displayed a typical cubic nanostructure. Figure 1c-e shows the EDS (electron diffraction spectroscopy) line scan and the corresponding STEM images of g-(Ni_{0.1}Mn_{0.9})HCF (Figure 1c), g-(Ni_{0.3}Mn_{0.7})HCF (Figure 1d) and g-(Ni_{0.5}Mn_{0.5})HCF (Figure 1e) particles. The results reveal that all samples display the similar trend of distribution of Ni and Mn in the particle, where the Ni concentration increases gradually from the center towards the surface, and the Mn concentration is low on the surface but increases near the center of the particle. The gradient distribution of the transition metal in the particle is further confirmed by EDS element mapping (Figure 1f, Figure S4). Compared with the homogeneous distribution of Fe, the Ni and Mn are heterogeneously distributed between the center and surface. However, the intensity ratio of Ni/Mn is different from the designed ratio and the ICP-OES results. It might be due to the different solubility between MnHCF ($K_{sp} \sim 10^{-3}$) and NiHCF ($K_{sp} \sim 10^{-16}$), leading to the formation of NiHCF particles that mixed with the gradient materials. As shown in Figure S5, g-(Ni_{0.1}Mn_{0.9})HCF comprises of microcubes of similar sizes. STEM images and the corresponding linear scan results of homogeneous (Ni_{0.1}Mn_{0.9})HCF and (Ni_{0.3}Mn_{0.7})HCF samples are shown in Figure S6, in which Ni, Fe and Mn elements exhibit a flat intensity along the linear scan, indicating the homogenous distribution of element from inner to the surface. These observations confirm that the synthesis method employed here can be applied to a wide range of Ni:Mn compounds to form a gradient particle with a controllable composition.

Figure 2 compares the electrochemical performance of gradient composites with different Ni:Mn ratios and the homogeneous phase of MnHCF and NiHCF in Na half-cells. Figure 2a shows the initial galvanostatic charge/discharge voltage profile of cycled cells at 0.2 C. NiHCF displays a voltage plateau at ~ 3.4 V during charge and ~ 3.2 V during discharge, which is associated with the redox reaction of $\text{Fe}^{2+/3+}-\text{C}\equiv\text{N}-\text{Ni}$. The initial charge and discharge capacities of NiHCF are 55 mAh/g and 60 mAh/g, respectively. Although the capacity exhibited by NiHCF is lower when compared with gradient materials and MnHCF, NiHCF retains nearly 100% of its capacity after 100 cycles at 0.2 C (Figure 2b), displaying superior cycling stability. For the MnHCF cathode, two plateaus are observed (Figure 2a): the voltage plateau at 3.4V / 3.2V for charge / discharge shows similar redox reactions as seen in NiHCF, and are attributed to the redox pair of $\text{Fe}^{2+/3+}-\text{C}\equiv\text{N}-\text{Mn}$. In addition, a higher voltage plateau at 3.7V / 3.5 V (Figure S7) for charge / discharge is related to the redox reaction of $\text{Fe}-\text{C}\equiv\text{N}-\text{Mn}^{2+/3+}$. Figure S8 shows the charge/discharge (Figure S8a) and differential capacities versus voltage (dQ/dv) curves (Figure S8b) of MnHCF cathodes during cycling. Structural reconstruction characteristics of loss of interstitial water from crystal structure causes the higher voltage plateau to decrease by 0.2V over initial cycling.

Owing to two active redox sites of $\text{Fe}^{2+/3+}$ and $\text{Mn}^{2+/3+}$ in $\text{Fe}-\text{C}\equiv\text{N}-\text{Mn}$, MnHCF exhibits the highest reversible capacity, however, its capacity retention is poor. As shown in Figure 2b, the discharge capacity of MnHCF decreases rapidly from 122 mAh/g to 64 mAh/g, corresponding to a capacity retention of a meagre 52.5% after 100 cycles. The voltage plateaus become shorter and a larger overpotential is observed upon cycling. These inferior electrochemical properties of MnHCF in liquid electrolytes are consistent with previous reports.²⁹

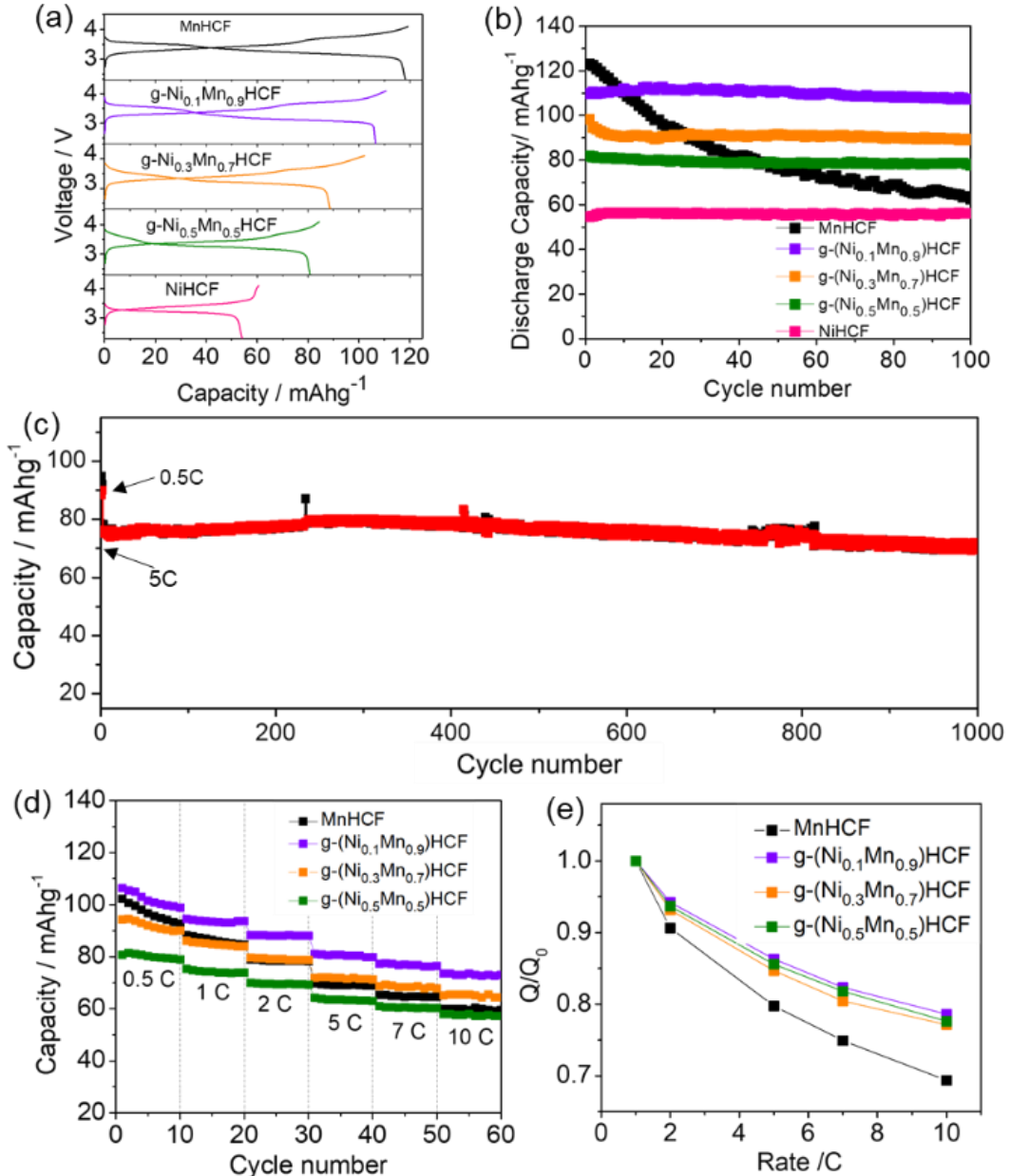


Figure 2 (a) Charge/discharge curves and (b) cycling performance of gradient material, MnHCF and NiHCF at 0.2 C; (c) long-term cycling of the typical g-(Ni_{0.3}Mn_{0.7})HCF at 5C; (d) rate capability and (e) normalized capacity of gradient materials at different C-rates.

Different Ni:Mn ratios in the concentration-gradient cathodes, bring about changes in the reversible capacity and the voltage plateau. The voltage profiles (Figure 2a) of g-(Ni_{0.5}Mn_{0.5})HCF, g-(Ni_{0.3}Mn_{0.7})HCF and g-(Ni_{0.1}Mn_{0.9})HCF reveal two plateaus at 3.4V / 3.2V and 3.7V / 3.5V when

cycled between 2.0-4.1 V. The presence of the 3.2 V plateau is indicative of the $\text{Fe}^{2+/3+}$ redox couple which delivers a similar capacity to the homogenous MnHCF and NiHCF, whereas the high voltage plateau (3.5V/3.7V) associated with the redox couple of $\text{Mn}^{2+/3+}$ becomes longer with the reduction of Ni in the particle. The reversible capacities (Figure 2b) of g-($\text{Ni}_{0.1}\text{Mn}_{0.9}$)HCF, g-($\text{Ni}_{0.3}\text{Mn}_{0.7}$)HCF and g-($\text{Ni}_{0.5}\text{Mn}_{0.5}$)HCF are 110 mAh g⁻¹, 98 mAh g⁻¹ and 82 mAh g⁻¹ at 0.2 C, respectively. It is seen that capacity decreased with the increasing Ni:Mn ratio and a lower Coulombic efficiency (C.E.) was seen in initial cycles, which might be attributed into the decomposition of electrolyte. The gradient-concentration materials showed a lower initial capacity than MnHCF, however, an improved cycling performance with a capacity retention of 95%, 93% and 96% after 100 cycles was observed, which is considerably higher than that of MnHCF (52.5%). Such a trend was expected since NiFCH has a better stability, whereas MnHCF a higher capacity, however, the ability of just a small addition of Ni to increase the stability so drastically was not anticipated. As shown in Figure S9, in comparison with the gradient materials, the non-gradient materials ($\text{Ni}_{0.1}\text{Mn}_{0.9}$)HCF and ($\text{Ni}_{0.3}\text{Mn}_{0.7}$)HCF display capacity retentions of 86% and 84% after 100 cycles, respectively. The long-term cycling stability was evaluated by galvanostatic charge/discharge tests at 0.5C for the first-two cycles and then at 5 C for 1000 cycles (Figure 2c). The g-($\text{Ni}_{0.3}\text{Mn}_{0.7}$)HCF cathode delivered a high capacity retention of 93% after 1000 cycles (The capacity retention was calculated based on the value of 5C in Figure 2c). Comparing the XRD patterns for this cathode (Figure S10) from before and after cycling showed that no apparent changes occurred after 1000 cycles, in accordance with the stable long-term cycling performance of the gradient composite.

The rate capability of the obtained materials was evaluated at different current densities ranging from 0.5 C to 10 C in the voltage range of 2.0 ~ 4.1 V at room temperature. As shown in

Figure 2d, the capacity of the MnHCF cathode decreased rapidly with increasing the current density from 100 mAh/g at 1 C to 60 mAh/g at 10 C. In contrast, the g-NiMnHCF samples maintained most of their capacity and showed excellent rate capabilities in a wide range of current densities. The separation of the potential (Figure S11) between charge and discharge increased slightly with increasing the C-rate, implying the weak polarization and overpotential during the electrochemical process. A discharge capacity of 110 mAh g⁻¹ and 100 mAh g⁻¹ was observed for the g-(Ni_{0.1}Mn_{0.9})HCF cathode at 0.5 C and 1 C, respectively, and decreased slightly with increasing the C-rate. The electrode exhibited a high capacity of 72 mAh g⁻¹ at 10 C, corresponding to a 78% capacity retention at 1 C. Although the g-(Ni_{0.5}Mn_{0.5})HCF cathode delivered the lowest specific capacity at 0.5 C due to the inactivity of Ni²⁺, it exhibited the least capacity decay with an increase in current density, indicating the excellent high-rate capability.

Figure 2e compares the normalized capacity (Q/Q_0) of the samples at different current densities. Q is the capacity at different C-rates, and Q_0 is the capacity of electrodes at 1 C. The normalized capacity of g-NiMnHCF was higher than that of the MnHCF cathode at current densities ranging from 2 C to 10 C. The g-(Ni_{0.5}Mn_{0.5})HCF cathode retained 78% of its capacity when cycled at 10 C against just the 67% retention MnHCF. This further supports the excellent electrochemical performance of gradient materials (g-(Ni_{0.1}Mn_{0.9})HCF, g-(Ni_{0.3}Mn_{0.7})HCF and g-(Ni_{0.5}Mn_{0.5})HCF) in terms of cycling stability and rate capability achieved, with minimal sacrifice of the specific capacity when compared with homogenous MnHCF. The high rate capability is determined by a fast ion diffusion and charge transfer in the electrode during the electrochemical process. The diffusion coefficient of Na⁺ (D_{Na^+}) in the cathode (g-(Ni_{0.1}Mn_{0.9})HCF and MnHCF) was estimated from cyclic voltammograms (CV) with varying scan speeds by the Randles–Sevcik method.³³⁻³⁴ As shown in Figure S12, the D_{Na^+} value in the g-(Ni_{0.1}Mn_{0.9})HCF cathode during

sodiation and desodiation was $4.8 \times 10^{-11} \text{ cm}^2 \text{ s}^{-1}$ and $5.9 \times 10^{-11} \text{ cm}^2 \text{ s}^{-1}$, respectively, which is higher than D_{Na^+} in the pure MnHCF cathode ($2.4 \times 10^{-11} \text{ cm}^2 \text{ s}^{-1}$ for sodiation and $3.8 \times 10^{-11} \text{ cm}^2 \text{ s}^{-1}$ for desodiation). Therefore, the gradient substitution by Ni enhanced the Na^+ diffusivity in the electrode, resulting into the faster rate capability.

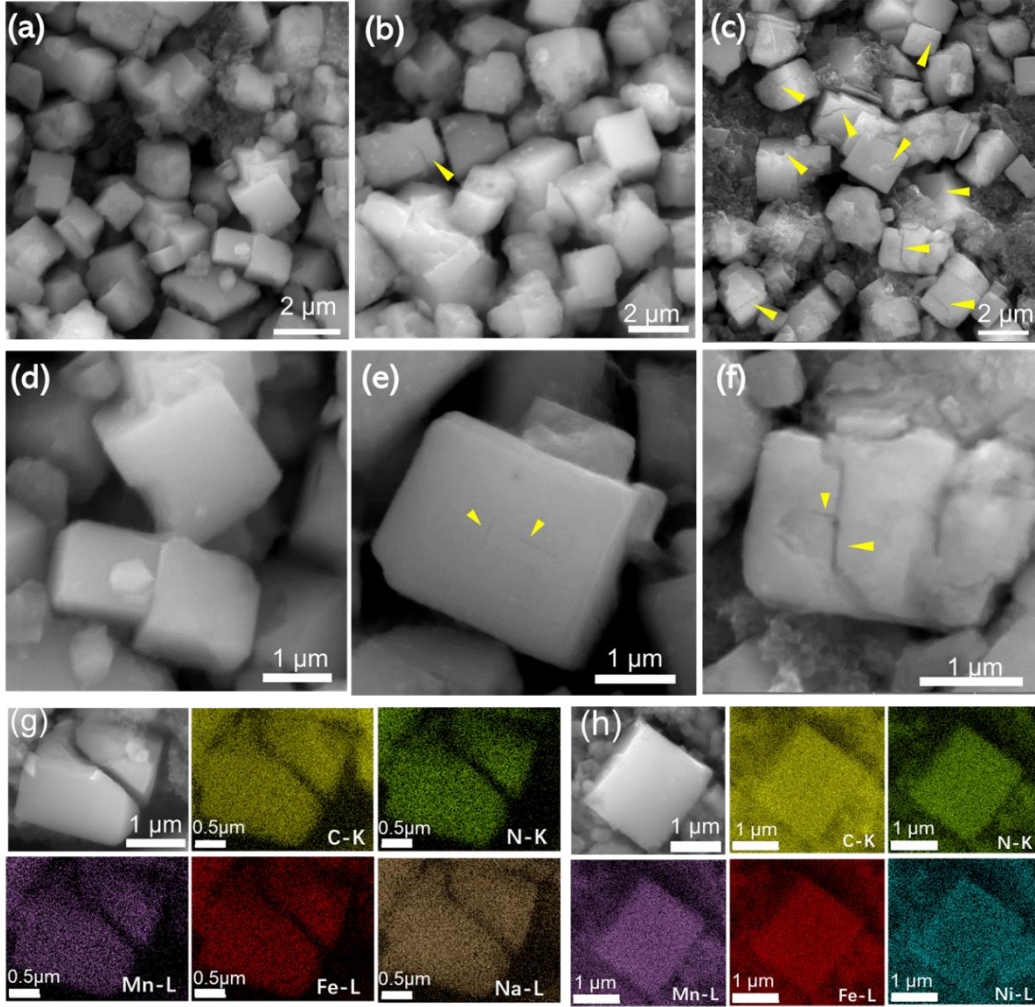


Figure 3 (a-c) Low magnification SEM images of MnHCF materials after (a) 10, (b) 20 and (c) 50 cycles. (d-f) High magnification SEM images of MnHCF materials after (d) 10, (e) 20 and (f) 50 cycles. (g-h) SEM images and element mapping of (g) MnHCF and (h) g-(Ni_{0.1}Mn_{0.9})HCF after 100 cycles.

Scanning electron microscopy (SEM) was performed to determine the initiation and propagation of fracture in the PBA cathodes upon cycling. Figure S13 shows the morphology of active particles for the MnHCF (Figure S13a) and g-(Ni_{0.1}Mn_{0.9})HCF (Figure S13b) cathodes before cycling. As shown in **Figure 3**, the MnHCF particles retained their cubic shape and size upon cycling, however, the morphology of their surface changed and became rougher/coarser. Such morphological changes can be attributed into the dissolution of Mn²⁺ into the organic electrolyte,²⁹ leading to corrosion of the surface. MnHCF active particles exhibited no obvious signs of fracture after 10 cycles, however small-scale crack initiation and propagation was observed from 20 cycles (Figure 3b and e). After 50 cycles (Figure 3c), fracture was observed in almost every particle. The cracks appeared on the face center of each particle. The crack width after 100 cycles (Figure 3g) was measured to be ~ 100 nm. These experimental observations can interpret the capacity decay that is seen in Figure 2b after 100 cycles. It is expected that the structural changes in the form of phase transitions and/or volume expansions during sodiation can induce strain/stress in the active particles, resulting in mechanical damage and capacity fade. Moreover, comparing the XRD patterns at different states of charge (Figure S14a) showed that splitting peaks at ~23.7° and 37.9° in the pristine electrode are merged into sharp single peaks at the charged state, due to the phase transformation from monoclinic to cubic. The peaks of the charged electrode shifted to a slightly lower angle, suggesting the expansion of the lattice during the Na⁺ extraction process. All diffraction peaks returned to their pristine state after complete sodiation, illustrating that the phase transformation was reversible during charge/discharge, however, the electrode suffered a ~8.5% volume change during this process (as determined by refining the XRD peaking with the Fullprof software), which is consistent with previous studies.²⁶ These structural changes would contribute to the fracture of the active particles. Such fracture

disrupts the electronic conductivity and ionic diffusion in the electrode, moreover corrosion causes parasitic side reactions on the newly formed surfaces, thus leading to a continuous capacity fade. In contrast, the gradient material g-(Ni_{0.1}Mn_{0.9})HCF cathode retained its structural integrity during cycling, as no obvious cracking was observed after 100 cycles (Figure 3h).

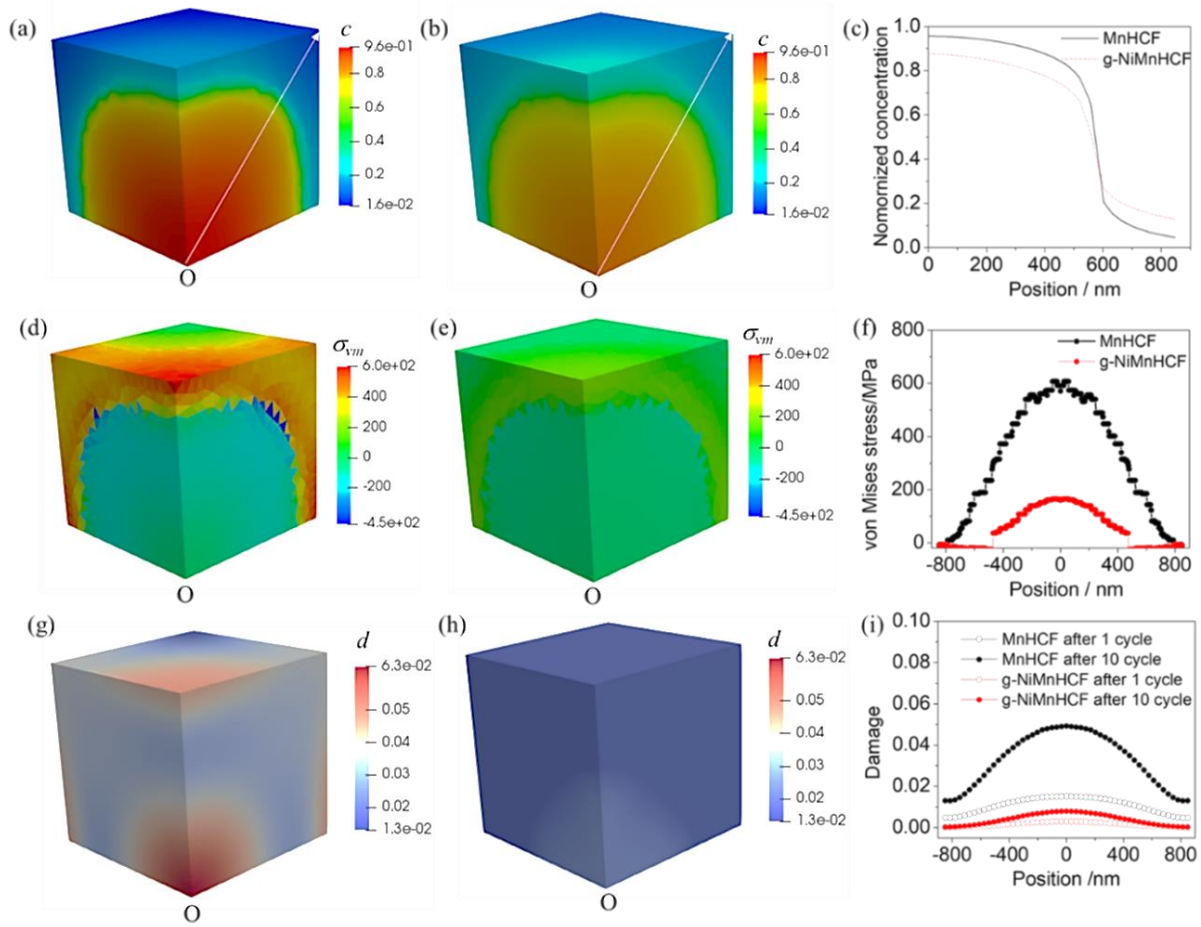


Figure 4. Chemomechanical simulation results showing damage evolution and stress generation in MnHCF and g-NiMnHCF during electrochemical cycling. (a)-(b) Concentration distribution in one-eighth unit cell at 50% state of charge (SOC) for (a) MnHCF and (b) g-NiMnHCF. (c) Concentration profiles from the center of the particle to the edge center of the top surface (along white arrows in a and b). (d)-(f) Modulated von Mises stress (σ_{vm}) distribution in MnHCF (d) and

g-NiMnHCF (e) during cycling. (f) Comparison of modulated von Mises stress profiles along the diagonal line on the top surface of MnHCF and g-NiMnHCF. (g)-(h) Damage distribution of MnHCF (g) and g-NiMnHCF (h) materials after 10 cycles respectively. (i) Comparison of damage profiles along the diagonal line on the top surface of MnHCF and g-NiMnHCF after 10 cycles.

To gain a thorough understanding of crack formation, finite element simulations were performed to model diffusion-induced stresses and damage in active particles during repeated electrochemical cycles using the model presented in Ref [35]. Considering symmetry, only one-eighth of the cubic particle was modelled. As shown in Figure S17a, the letter “O” marks the center of the particle. Two different compositions MnHCF and g-NiMnHCF were considered. Since both materials undergo a two-phase reaction mechanism (monoclinic to cubic phase transition) during sodiation/desodiation, at each intermediate state the active particle was treated as a core-shell-like cubic structure, where the core region was the pristine part and the shell region was the de-sodiated region. Contour plots (**Figure 4a and b**) of the normalized Na^+ concentration (C_{Na^+}) obtained by the concentration-dependent diffusivity equation (as shown in Eq-S1) show a sharp phase reaction and steep distribution of C_{Na^+} , which would cause an abrupt change of stresses in the two-phase regions; where the core region is under compressive (negative) stress while the shell is under tensile (positive) stress during desodiation (as shown Figure 4d and e). Therefore, there is a jump of the hydrostatic stress ($\sigma_h = \text{tr}(\boldsymbol{\sigma})/3$) at the de-sodiation reaction front. Figure 4c compares the diagonal distributions of C_{Na^+} in MnHCF and g- NiMnHCF. The profile for C_{Na^+} is less steep for g-NiMnHCF than for MnHCF due to the faster diffusion of Na^+ in g-NiMnHCF. It should also be noted that g-NiMnHCF has a much lower volume expansion (0.29%) than that of MnHCF (8.5%). Both factors lead to a significantly lower Von Mises stress than in MnHCF.

The von Mises stress (σ_v) distribution was investigated since it's the main factor contributing to plastic deformation and fracture. Figure 4(d-e) depicts the contour plots of the modulated von Mises stress ($\sigma_{vm} = \text{sign}(\sigma_h) \times \sigma_v$ where $\text{sign}(\sigma_h)$ represents the sign function of σ_h and its value is 1 when $\sigma_h > 0$ and -1 when $\sigma_h < 0$) for MnHCF and g-NiMnHCF at a 50% state of charge (SOC). The maximum value for σ_v is located near the core(pristine)-shell(sodiated) interface. Figure 4f compares the σ_{vm} distributions along the diagonal direction on the surfaces of the particle. The maximum σ_v is also observed at the center of the cubic particles, however, there is an appreciable difference in the magnitude of the observed stress in MnHCF (607 MPa) and g-NiMnHCF (165 MPa). The maximum σ_v in MnHCF is nearly 4 times of that in g-NiMnHCF. It should also be noted that for g-NiMnHCF, the region under tension is of very limited volume contrary to what occurs in MnHCF (Figure 4f). Almost the entire external surface of MnHCF is under tension whereas in g-NiMnHCF only the region near the vertex is in compression.

The damage evolution is further simulated to understand the impact of different compositions on the mechanical degradation of the particles. Since no pre-existing cracks or flaws were considered in the simulation, the damage profiles are similar during initial cycling, for both homogeneous and gradient cathodes, as shown in Figure S18 and Figure 4g-h, which demonstrate the damage profiles of MnHCF and g-NiMnHCF after the 1st and 10th cycle, respectively. A scalar phase-field variable d ranging from 0 to 1 ($d=0$ for unbroken/intact state, and $d=1$ for fully broken damaged state) is defined. Damage in MnHCF was localized near the center of the external surfaces as well as near the center of the particles, while damage in g-NiMnHCF particles, was confined to the center of the cell (Figure 4h). Figure S18 shows that the maximum damage increased upon cycling for both MnHCF and g-NiMnHCF, however, the damage values at the particle center and surface center of MnHCF increased to 6.35% and 4.83% after 10 cycles, which

is much higher when compared with g-NiMnHCF (1.96% and 0.79%, respectively). g-NiMnHCF exhibited alleviation of accumulated damage in the vicinity of the face center. Figure 4i shows the damage distribution of MnHCF and g-NiMnHCF along the diagonal line on the top surface after 1 and 10 cycles, respectively. Similar damage profiles were observed, however, the magnitudes were significantly different; the maximum damage values for MnHCF being 1.52% and 4.92% and for g-NiMnHCF being 0.31% and 0.80% after 1 and 10 cycles, respectively. Both homogenous and concentration-gradient particles demonstrate about a 3-fold increase in maximum damage over the 1st and 10th cycle, even though for the g-NiMnHCF it is negligible. Fracture is likely to occur in regions showing increased damage upon cycling, and therefore if the simulation for the homogeneous materials was run over 20 cycles, cracks would nucleate as in the experimental images. However, due to computational costs simulations were stopped after 10 cycles. In Figure 4 it is seen that the predicted damage value is significantly low in g-NiMnHCF particles, and no cracks were anticipated. Therefore, g-NiMnHCF has a much better mechanical performance than MnHCF.

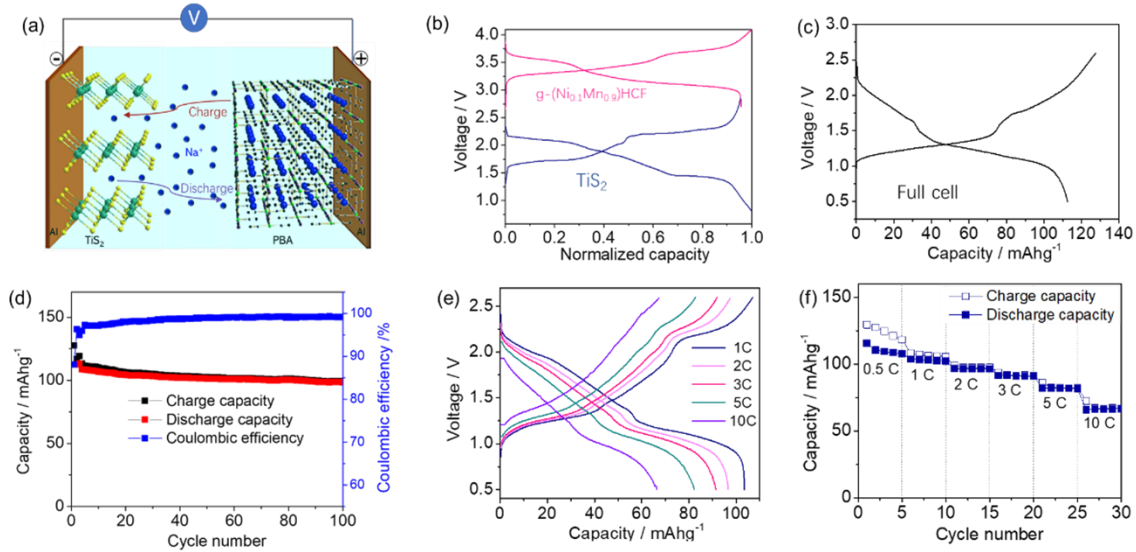


Figure. 5 (a) Schematic mechanism of full cell that using g-NiMnHCF as cathode and TiS₂ as anode. (b) Charge/discharge profiles of g-Ni_{0.1}Mn_{0.9}HCF and TiS₂ in half cell. (c) The first charge/discharge curves of the full cell using g-Ni_{0.1}Mn_{0.9}HCF as cathode and TiS₂ as anode. (d) Cycling performance of the full cell at 0.5 C. (e) Charge/discharge curve and rate capability of the full cell at different C-rate. (f) The capacity was calculated by the cathode mass.

Sodium metal is not an ideal anode for commercial batteries due to its high reactivity with the electrolyte and dendrite formation³⁶, which results in safety issues. Carbon-based materials such as hard carbon and graphite are commonly used as anodes for Na-ion full cells. However, the potential plateau of hard carbon is close to the plating potential of Na, leading to the formation of Na dendrites during the charge process.³⁷⁻³⁸ In testing the present gradient PBAs in a full cell, graphitic anodes were considered first, which cycle only in glyme electrolyte. In Figure S15a and b it is seen that a capacity of 125 mAh g⁻¹ and a low initial Coulombic efficiency (C.E.) of 70% were obtained after the first cycle. In Figure S15c it is seen that although the g-(Ni_{0.1}Mn_{0.9})HCF/graphite full cell displayed a stable discharge capacity within 100 cycles, it delivered a low C.E. of 50%. Therefore, activation of the graphite anode is required before coupling with the cathode to assemble a full cell. Our previous research demonstrated that TiS₂/Na half-cells presented superior electrochemical performance in carbonate-based electrolyte. Herein, therefore a layered-type TiS₂ with particle size of ~ 5 μm (Figure S16b) was chosen as the anode. The strong (001) diffraction peak (Figure S16a) implied a highly preferred orientation along the *c*-axis direction and good S-Ti-S layer stacks. Using TiS₂ in a half Na-ion cell allowed to obtain a high reversible capacity of 200 mAh g⁻¹ at 0.5C, initial Coulombic efficiency (95%), cycling stability and rate capability (157 mAh g⁻¹ at 5 C, 122 mAh g⁻¹ at 10 C), as seen in Figure S16c-d.

A full cell, as illustrated in **Figure 5a**, was therefore assembled by using g-(Ni_{0.1}Mn_{0.9})HCF as the cathode, TiS₂ as the anode and 1 M NaPF₆ in EC/DMC with 5% FEC as the electrolyte. Figure 5b shows charge/discharge profiles of voltage vs. normalized capacity for g-(Ni_{0.1}Mn_{0.9})HCF and TiS₂ electrodes. The voltage difference between the two electrodes determines the working voltage of the full cell. As shown in Figure 5c, the full cell presents two potential profiles at ~1.2 V and ~2.1V. The initial charge and discharge capacities were 127 mA h g⁻¹ and 112 mA h g⁻¹ at 0.5 C in the potential range of 0.5-2.6V, exhibiting a high initial C.E. of 88.1%. High C.E. benefits from the highly reversible nature of both the cathode and anode materials. The cycling stability of the full cell was examined at 1C. As shown in Figure 5d, the reversible capacity of the cathode in the full cell reached 110 mA h g⁻¹ and a capacity retention of 87.5% was observed over 100 cycles. Figure 5(e-f) shows that the capacity decreased slightly as the rate increased from 0.5 C to 10 C. At 5 C and 10 C, it still achieved a capacity of 88 mAh g⁻¹ and 70 mAh g⁻¹, implying excellent rate capability. Comparing with the performance of full cells reported in previous studies (Table S3), our results show a superior rate capability, initial C.E and stability, which indicates a great advance over the state-of-the-art of sodium-ion batteries. The output voltage of the full cell is lower than the organic cell using carbon and alloying anode, but it is in the stable potential window of the aqueous electrolyte, making it feasible to run in an aqueous electrolyte. The aqueous SIBs based on these materials will be studied in-depth in further work.

In conclusion, concentration-gradient materials g-NiMnHCF were successfully synthesized via a facile co-precipitation process, resulting in a Ni rich shell and Mn core. The expansion of NiHCF upon sodiation is less than 1%, whereas that of MnHCF is 8.5%, hence this gradient microstructure allows to buffer the core volume changes. The as-obtained gradient microstructure cathodes exhibited outstanding cycling stability and rate capability, when compared with the

homogenous MnHCF cathodes. SEM images revealed that after twenty cycles cracks initiated and propagated at the center of the MnHCF particles, but no damage occurred in the g-NiMnHCF. The superior electrochemical performance of g-NiMnHCF could therefore be attributed to its stable structure and fast ionic diffusivity, which reduce the mechanical degradation induced by diffusion at the reaction front during charge/discharge. The experimental data were interpreted with phase field modeling which showed that g-NiMnHCF experiences lower von Mises stresses and hydrostatic stress levels and negligible damage, while MnHCF with a uniform composition undergoes higher stresses, and the damage tends to localize at regions close to the particle center and face centers. The maximum damage for MnHCF is more than 3 times as that for g-NiMnHCF. As a result, g-NiMnHCF shows better damage tolerance and its mechanical degradation due to excessive stresses can be effectively retarded. In concluding, a full cell using TiS_2 as the anode and g-NiMnHCF as the cathode was shown to have an outstanding initial Coulombic efficiency, capacity retention and rate capability, demonstrating potential practical applications in energy storage. Therefore, designing gradient composition materials is an effective approach to improve the stability of PBA cathodes. We also believe that this approach can be reasonably extended to other electrode materials to solve the mechanical degradation in LIBs and SIBs.

Supporting Information.

The Supporting Information is available free of charge on the ACS Publications website at DOI:xxxx.

Experimental details of preparation, characterizations and simulations. Additional figures and tables showing TGA, XRD, ICP, SEM, and simulation results.

Notes

The authors declare no competing financial interest.

Acknowledgements

The authors are grateful to the National Science Foundation for supporting this work through the CMMI grant (CMMI-1762602).

References

1. Goodenough, J. B.; Park, K.-S., The Li-Ion Rechargeable Battery: A Perspective. *J. Am. Chem. Soc.* **2013**, *135*, 1167-1176.
2. Scrosati, B.; Hassoun, J.; Sun, Y. K., Lithium-ion batteries. A look into the future. *Energy Environ. Sci.* **2011**, *4*, 3287-3295.
3. Zuo, Y. X.; Li, B. A.; Jiang, N.; Chu, W. S.; Zhang, H.; Zou, R. Q.; Xia, D. G., A High-Capacity O2-Type Li-Rich Cathode Material with a Single-Layer Li_2MnO_3 Superstructure. *Adv. Mater.* **2018**, *30*, 1707255.
4. Hwang, J. Y.; Myung, S. T.; Sun, Y. K., Sodium-ion Batteries: Present and Future. *Chem. Soc. Rev.* **2017**, *46*, 3529-3614.
5. Hu, Y. S.; Komaba, S.; Forsyth, M.; Johnson, C.; Rojo, T., A New Emerging Technology: Na-Ion Batteries. *Small Methods* **2019**, *3*, 1900184.
6. Ebner, M.; Marone, F.; Stampanoni, M.; Wood, V., Visualization and Quantification of Electrochemical and Mechanical Degradation in Li Ion Batteries. *Science* **2013**, *342*, 716-720.
7. Aifantis, K. E.; Huang, T.; Hackney, S. A.; Sarakonsri, T.; Yu, A. S., Capacity fade in Sn-C nanopowder anodes due to fracture. *J. Power Sources* **2012**, *197*, 246-252.
8. Aifantis, K. E.; Hackney, S. A., Mechanical Stability for Nanostructured Sn- and Si-Based Anodes. *J. Power Sources* **2011**, *196*, 2122-2127.

9. Aifantis, K. E.; Dempsey, J. P., Stable Crack Growth in Nanostructured Li-batteries. *J. Power Sources* **2005**, *143*, 203-211.
10. Xu, J. G.; Deshpande, R. D.; Pan, J.; Cheng, Y. T.; Battaglia, V. S., Electrode Side Reactions, Capacity Loss and Mechanical Degradation in Lithium-Ion Batteries. *J. Electrochem. Soc.* **2015**, *162*, A2026-A2035.
11. Aifantis, K. E.; Haycock, M.; Sanders, P.; Hackney, S. A., Fracture of Nanostructured Sn/C Anodes during Li-insertion. *Mat Sci Eng a-Struct* **2011**, *529*, 55-61.
12. McGrogan, F. P.; Raja, S. N.; Chiang, Y. M.; Van Vliet, K. J., Electrochemomechanical Fatigue: Decoupling Mechanisms of Fracture- Induced Performance Degradation in $\text{Li}_x\text{Mn}_2\text{O}_4$. *J. Electrochem. Soc.* **2018**, *165*, A2458-A2466.
13. Qi, Y.; Xu, Q. C.; Van der Ven, A., Chemically Induced Crack Instability When Electrodes Fracture. *J. Electrochem. Soc.* **2012**, *159*, A1838-A1843.
14. Hao, X. G.; Lin, X. K.; Lu, W.; Bartlett, B. M., Oxygen Vacancies Lead to Loss of Domain Order, Particle Fracture, and Rapid Capacity Fade in Lithium Manganospinel (LiMn_2O_4) Batteries. *ACS Appl. Mater. Interfaces* **2014**, *6*, 10849-10857.
15. Qu, M.; Woodford, W. H.; Maloney, J. M.; Carter, W. C.; Chiang, Y. M.; Van Vliet, K. J., Nanomechanical Quantification of Elastic, Plastic, and Fracture Properties of LiCoO_2 . *Adv. Energy Mater.* **2012**, *2*, 940-944.
16. Yu, Y. S.; Kim, C.; Shapiro, D. A.; Farmand, M.; Qian, D.; Tyliszczak, T.; Kilcoyne, A. L. D.; Celestre, R.; Marchesini, S.; Joseph, J.; Denes, P.; Warwick, T.; Strobridge, F. C.; Grey, C. P.; Padmore, H.; Meng, Y. S.; Kostecki, R.; Cabana, J., Dependence on Crystal Size of the Nanoscale Chemical Phase Distribution and Fracture in Li_xFePO_4 . *Nano Lett.* **2015**, *15*, 4282-4288.

17. Yan, P. F.; Zheng, J. M.; Gu, M.; Xiao, J.; Zhang, J. G.; Wang, C. M., Intragranular Cracking as a Critical Barrier for High-Voltage Usage of Layer-Structured Cathode for Lithium-Ion Batteries. *Nat. Commun.* **2017**, *8*, 14101.
18. Xu, B.; Meng, S., Factors Affecting Li Mobility in Spinel LiMn_2O_4 -A First-Principles Study by GGA and GGA Plus U methods. *J. Power Sources* **2010**, *195*, 4971-4976.
19. Wang, D. Y.; Wu, X. D.; Wang, Z. X.; Chen, L. Q., Cracking Causing Cyclic Instability of LiFePO_4 Cathode Material. *J. Power Sources* **2005**, *140*, 125-128.
20. Wang, J. W.; Liu, X. H.; Mao, S. X.; Huang, J. Y., Microstructural Evolution of Tin Nanoparticles during In Situ Sodium Insertion and Extraction. *Nano Lett.* **2012**, *12*, 5897-5902.
21. Gu, M.; Kushima, A.; Shao, Y. Y.; Zhang, J. G.; Liu, J.; Browning, N. D.; Li, J.; Wang, C. M., Probing the Failure Mechanism of SnO_2 Nanowires for Sodium-Ion Batteries. *Nano Lett.* **2013**, *13*, 5203-5211.
22. You, Y.; Wu, X. L.; Yin, Y. X.; Guo, Y. G., High-Quality Prussian Blue Crystals as Superior Cathode Materials for Room-Temperature Sodium-Ion Batteries. *Energy Environ. Sci.* **2014**, *7*, 1643-1647.
23. Wang, L.; Lu, Y. H.; Liu, J.; Xu, M. W.; Cheng, J. G.; Zhang, D. W.; Goodenough, J. B., A Superior Low-Cost Cathode for a Na-Ion Battery. *Angew Chem Int Edit* **2013**, *52*, 1964-1967.
24. Lu, Y. H.; Wang, L.; Cheng, J. G.; Goodenough, J. B., Prussian Blue: a New Framework of Electrode Materials for Sodium Batteries. *Chem. Commun.* **2012**, *48*, 6544-6546.
25. Xiao, P. H.; Song, J.; Wang, L.; Goodenough, J. B.; Henkelman, G., Theoretical Study of the Structural Evolution of a $\text{Na}_2\text{FeMn}(\text{CN})_6$ Cathode upon Na Intercalation. *Chem. Mater.* **2015**, *27*, 3763-3768.

26. Song, J.; Wang, L.; Lu, Y. H.; Liu, J.; Guo, B. K.; Xiao, P. H.; Lee, J. J.; Yang, X. Q.; Henkelman, G.; Goodenough, J. B., Removal of Interstitial H₂O in Hexacyanometallates for a Superior Cathode of a Sodium-Ion Battery. *J. Am. Chem. Soc.* **2015**, *137*, 2658-2664.
27. Pan, H. L.; Hu, Y. S.; Chen, L. Q., Room-Temperature Stationary Sodium-Ion Batteries For Large-Scale Electric Energy Storage. *Energy Environ. Sci.* **2013**, *6*, 2338-2360.
28. Matsuda, T.; Takachi, M.; Moritomo, Y., A Sodium Manganese Ferrocyanide Thin Film For Na-Ion Batteries. *Chem. Commun.* **2013**, *49*, 2750-2752.
29. Gao, H. C.; Xin, S.; Xue, L. G.; Goodenough, J. B., Stabilizing a High-Energy-Density Rechargeable Sodium Battery with a Solid Electrolyte. *Chem-US* **2018**, *4*, 833-844.
30. Yang, D. Z.; Xu, J.; Liao, X. Z.; He, Y. S.; Liu, H. M.; Ma, Z. F., Structure Optimization of Prussian Blue Analogue Cathode Materials for Advanced Sodium Ion Batteries. *Chem. Commun.* **2014**, *50*, 13377-13380.
31. Moritomo, Y.; Urase, S.; Shibata, T., Enhanced Battery Performance in Manganese Hexacyanoferrate by Partial Substitution. *Electrochim. Acta* **2016**, *210*, 963-969.
32. Moritomo, Y.; Wakaume, K.; Takachi, M.; Zhu, X. H.; Kamioka, H., Li⁺ Intercalation of Manganese Ferrocyanide as Investigated by In situ Valence-Differential Absorption Spectroscopy. *J. Phys. Soc. Jpn.* **2013**, *82*, 094710.
33. Tang, K.; Yu, X. Q.; Sun, J. P.; Li, H.; Huang, X. J., Kinetic analysis on LiFePO₄ thin films by CV, GITT, and EIS. *Electrochim. Acta* **2011**, *56*, 4869-4875.
34. Rui, X. H.; Ding, N.; Liu, J.; Li, C.; Chen, C. H., Analysis of the Chemical Diffusion Coefficient of Lithium Ions in Li₃V₂(PO₄)₃ Cathode Material. *Electrochim. Acta* **2010**, *55*, 2384-2390.

35. Rethore, J.; Zheng, H.; Li, H.; Li, J. J.; Aifantis, K. E., A Multiphysics Model that can Capture Crack Patterns in Si Thin Films Based on Their Microstructure. *J. Power Sources* **2018**, *400*, 383-391.
36. Zhao, Y.; Adair, K. R.; Sun, X. L., Recent Developments and Insights into the Understanding of Na Metal Anodes for Na-Metal Batteries. *Energy Environ. Sci.* **2018**, *11*, 2673-2695.
37. Liu, T.; Zhang, Y.; Jiang, Z.; Zeng, X.; Ji, J.; Li, Z.; Gao, X.; Sun, M.; Lin, Z.; Ling, M.; Zheng, J.; Liang, C., Exploring Competitive Features of Stationary Sodium Ion Batteries for Electrochemical Energy Storage. *Energy Environ. Sci.* **2019**, *12*, 1512-1533.
38. Jache, B.; Adelhelm, P., Use of Graphite as a Highly Reversible Electrode with Superior Cycle Life for Sodium-Ion Batteries by Making Use of Co-Intercalation Phenomena. *Angew Chem Int Edit* **2014**, *53*, 10169-10173.